PAPER

Synthesis and atomic scale characterization of Er_2O_3 nanoparticles: enhancement of magnetic properties and changes in the local structure

IOP Publishing Nanotechnology
Nanotechnology **29** (2018) 205704 (8pp) https://doi.org/10.1088/1361-6528/aab3f8

Synthesis and atomic scale characterization of Er_2O_3 nanoparticles: enhancement of magnetic properties and changes in the local structure

Eduardo L Corrêa[1], Brianna Bosch-Santos[1], Rafael S Freitas[2], Maria da Penha A Potiens[1], Mitiko Saiki[1] and Artur W Carbonari[1]

[1] Instituto de Pesquisas Energéticas e Nucleares, Universidade de São Paulo, São Paulo, Brazil
[2] Instituto de Física, Universidade de São Paulo, São Paulo, Brazil

E-mail: eduardo.correa@usp.br

Received 27 December 2017, revised 20 February 2018
Accepted for publication 5 March 2018
Published 22 March 2018

Abstract

In the investigation reported in this paper a modified thermal decomposition method was developed to produce very small Er_2O_3 nanoparticles (NPs). Particles structure, shape and size were characterized by x-ray diffraction and transmission electron microscopy which showed that the synthesis by thermal decomposition under O_2 atmosphere produced very small and monodisperse NPs, allowing the investigation of finite-size and surface effects. Results of magnetization measurements showed that the smallest particles present the highest values of susceptibility that decrease as particle size increases. Specific heat measurements indicate that the sample with the smallest NPs (diameter ~5 nm) has a Néel temperature of 0.54 K. The local structure of particles was investigated by measurements of hyperfine interactions with perturbed angular correlation spectroscopy using ^{111}Cd as probe nuclei replacing the cationic sites. Results showed that the relative population of sites 8b increases in both the core and surface layer of particles.

Keywords: nanoparticles, PAC spectroscopy, Er_2O_3, magnetization, synthesis of nanoparticles, thermal decomposition

(Some figures may appear in colour only in the online journal)

1. Introduction

Rare earth nanoparticles (NPs) are good candidates for both medicine and technological applications [1–3], mainly because of their reduced dimensions as well as their peculiar magnetic properties when compared to bulk materials. Examples are: change in temperature in which the paramagnetic to antiferromagnetic (AFM) transition occurs and an optical band-gap shift, both probable consequences of particles finite-size effect [4, 5]. Structural and magnetic properties of erbium oxide NPs (Er_2O_3-NPs) were studied in the past due to their potential technological applications [6, 7]. Narang *et al* [8] and moon *et al* [9] presented a comprehensive study about the magnetic properties of Er_2O_3-NPs, including the Néel temperature (T_N) shift with the NP size and the mechanism for the dominant AFM coupling, which they attribute to superexchange interactions via the neighboring oxygen ion (Er–O–Er).

However, the presence of NPs with average size higher than 40 nm prevents the observation and, consequently, the analysis of the finite-size effects in Narang's study [8].

In the present paper, Er_2O_3-NP samples were prepared by the thermal decomposition method, which is known for producing very small particles with a narrow size distribution. This method also allows the synthesis of NPs with different shapes and can be used to produce metallic, oxides, core–shell structures and metal alloys NPs [10]. Er_2O_3-NPs were characterized by magnetization measurements to investigate

magnetic properties while their crystalline structure and morphology were characterized by x-ray diffraction (XRD) and transmission electron microscopy (TEM), respectively. A nuclear technique with atomic resolution, the perturbed angular correlation (PAC) spectroscopy, using ^{111}In(^{111}Cd) as probe nuclei, was used to investigate the local structure around the probes by measuring hyperfine interactions, in particular, the electric quadrupole interactions (EQI) as a function of temperature. EQI allows the study of structural phase transitions, oxidation reactions and electronic structure around the probe nuclei within an atomic range [11].

2. Experimental procedure

2.1. NPs synthesis

Samples of Er_2O_3-NPs were obtained using the traditional thermal decomposition with a modification in which 20 ml of diphenyl ether, 4 mmol of oleylamine, 6 mmol of oleic acid and 10 mmol of 1,2-octanediol were mixed with 2 mmol of erbium acetate. In this method metal complexes are reduced and/or decomposed using high boiling point ethers in the presence of oleic acid, oleylamine and 1,2-octanediol. The role of each reagent used in this method is not fully understood, possibly due to different roles and various possible interactions between metal precursor and each reagent [12]. A small volume of radioactive $^{111}InCl_3$ solution was added to the initial mixed solution during the NPs preparation to later on perform PAC measurements. Usually, the production of Fe_3O_4-NPs by thermal decomposition takes about 2 h [10, 13]. However, the first synthesis of Er_2O_3-NPs occurred after 30 h of solution magnetic stirring and heating at 573 K. In order to reduce the reaction time, an additional step was introduced by using an O_2 atmosphere flux during synthesis. With this improvement the reaction time was reduced to 6 h. After cooling at room temperature, 20 ml of a mix of methanol and ethanol (proportion of 1:2) were added to the solution, which was centrifuged for two hours at 5000 RPM. NPs were obtained after washing the sedimentation using 10 ml of methanol in ultrasound equipment in order to remove the excess of organic material (surfactant). This procedure was repeated three times. The resulting powder was dried under low pressure (about 1 kPa) for 24 h. At this point, the NPs were capped by organic material and the sample was divided into two parts: the first part (hereafter referred as sample 1) was annealed at 573 K in air for 10 h to reduce the organic material around NPs to obtain a better XRD spectrum while the second part (sample 2) was annealed at 873 K also in air for 10 h. According to a previous study this annealing temperature is enough to remove almost all organic material without drastically changing particles size and shape, allowing a better analysis of PAC spectroscopy results [14]. A commercial powder (sample 3), purchased from Sigma-Aldrich (99.9% purity, trace metals basis, 289248 Aldrich), was used for comparison. After the ^{111}In decay to safe levels, samples were characterized by XRD, TEM and magnetization measurements.

2.2. NPs structural and magnetic characterization

TEM was performed to characterize the material in term of NPs' shape, size and size distribution. XRD results were analyzed by the Rietveld method to check the crystal structure of NPs. The magnetic measurements were carried out in a magnetometer with a superconducting quantum interference device sensor (MPMS-XL, Quantum Design). Field-cooled (FC) and zero field-cooled (ZFC) curves were obtained by applying a magnetic field of 100 Oe and changing the temperature from 2 to 300 K. Magnetization as function of the applied magnetic field was made at 2 K, from 0 to 70 kOe. The specific heat data were obtained with a Quantum Design Dynacool system using a standard semi-adiabatic heat pulse technique under magnetic fields up to 9 T and temperatures down to 0.13 K. The addendum heat capacity was measured separately and then subtracted. Erbium concentration and the presence of possible impurities in each sample were evaluated by the method of neutron activation analysis (NAA) [15]. In this technique, about 5 mg of each Er2O3-NP sample was irradiated under a thermal neutron flux of $1.9 \times 10^{12}\,\mathrm{n\,cm^{-2}\,s^{-1}}$ for 1 min. The 308.29 keV gamma emitted by ^{171}Er isotope was measured in a Canberra hyperpure Ge detector connected to a DAS 1000 digital spectrum analyzer. Erbium concentration in each sample was calculated by comparative method.

PAC measurements were carried out using ^{111}Cd as probe nuclei, which are produced after the decay of ^{111}In, in a spectrometer with four BaF_2 detectors associated with a slow-fast setup used to measure delayed gamma–gamma coincidences. In this technique two gamma rays in cascade, emitted as result of the decay from the excited levels of probe nuclei, are detected. Gamma radiation angular correlation is perturbed by the interaction between intermediate nuclear state moment and extra nuclear fields. A homemade software was used to process the coincidence spectra to obtain the spin rotation function $R(t) = A_{22}G_{22}(t)$, where A_{22} is the anisotropy factor and $G_{22}(t)$ is the perturbation function. $G_{22}(t)$ takes into account the hyperfine interactions and can be modeled in terms of theoretical functions: electric quadrupole and/or magnetic dipole interactions. The perturbation function $G_{22}(t)$, specifically, contains detailed information about the hyperfine interaction and its measurement allows the determination of the Larmor frequency $\omega_L = \mu_N g B_{hf}/\hbar$ for magnetic dipole interactions, the nuclear quadrupole frequency $\nu_Q = eQV_{zz}/h$, and asymmetry parameter $\eta = (V_{xx} - V_{yy})/V_{zz}$. In the equations μ_N is the nuclear magnetron, g and Q are the g-factor and the electric quadrupole moment of the probe nucleus, respectively, and V_{kk} ($k = x, y, z$) denote the main components of the electric field gradient (efg) tensor. The perturbation function $G_{22}(t)$ allows the determination of the efg and the magnetic hyperfine field (B_{hf}). More information about the experimental method and PAC spectroscopy can be found elsewhere [16, 17].

In this study PAC measurements were carried out at different temperatures: 10, 77, 119, 250, 300 and 400 K.

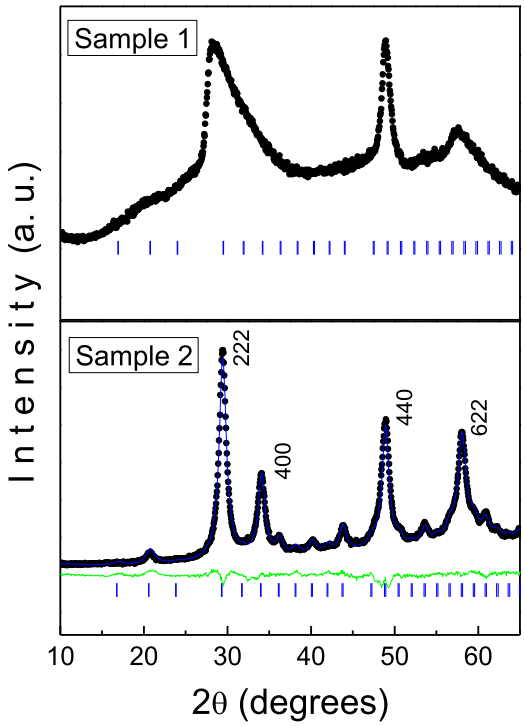

Figure 1. XRD patterns for samples 1 (annealed at 573 K for 10 h) and 2 (annealed at 873 K for 10 h). Organic material creates amorphous spectra which, along with the small size of the particles, widen the peaks. Blue bars are the expected peaks position for Er_2O_3, and green line is the quality of the theoretical adjust to the experimental data.

3. Results and discussion

3.1. NPs structural properties—XRD and TEM

XRD pattern at room temperature for NPs samples are displayed in figure 1. Blue bars are the expected peaks position for Er_2O_3.

XRD pattern for sample 1 shows large and non-defined peaks (figure 1), indicating large quantity of organic material and very small NP. Peaks become narrow and well defined with larger particles and less organic material, which can be obtained by annealing the sample. Therefore, only the spectrum for sample 2 could be analyzed by the Rietveld method, and results show that sample 2 has crystallized in the cubic C-type structure with *Ia*-3 space group (bixbiyte). The fit yielded lattice parameters $a = b = c = 10.531(5)$ Å, with a profile *R*-factor (Rp) [18] of 4.11, in accordance with those presented in previous studies, $a = b = c = 10.536(1)$ Å [19].

The unit cell of Er_2O_3 bixbyite structure contains 48 oxygen and 32 erbium atoms sitting on two non-equivalent sites: site 24d, occupied by 24 erbium atoms with C_2 symmetry and site 8b, occupied by 8 erbium atoms with D_{3d} symmetry [20].

An estimate of the crystallite size D can be obtained using Scherrer equation as follows [21]

$$D = \frac{K\lambda}{\beta \cos \theta},$$

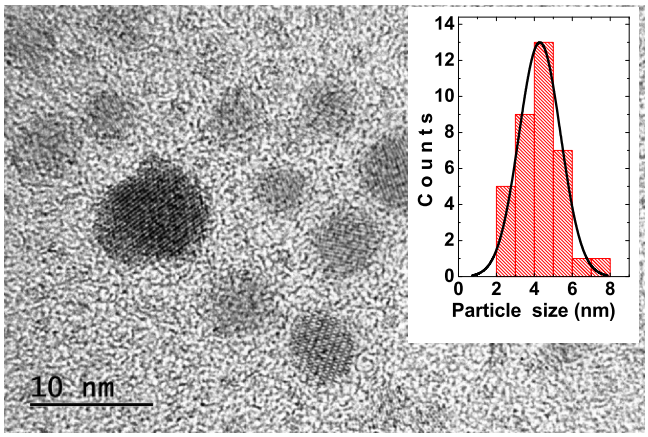

Figure 2. Sample 1 TEM image. The inset displays the histogram of NPs size distribution. The average size is 4.29 nm with $\sigma = 1.1$ nm.

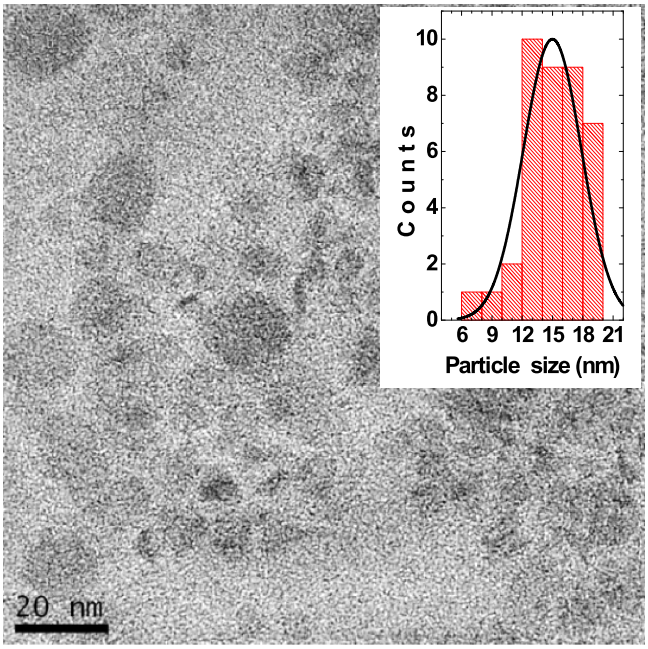

Figure 3. Sample 2 TEM image. The inset displays the histogram of NPs size distribution. The average size is 14.99 nm with $\sigma = 2.9$ nm.

where $K = 0.93$, λ, β and θ are the shape factor, x-ray wavelength (0.154 18 nm for Cu-Kα), full width at half-maximum of the diffraction peak and Bragg diffraction angle, respectively. For sample 2 the D value is ~8 nm. As the peaks in the x-ray diffractogram of sample 1 are very broad, it was not possible to use Scherrer's formula to obtain a reliable estimate of the crystallite sizes.

TEM results show spherical-shape NP as displayed in figures 2 and 3, respectively, for samples 1 and 2. The insets in the figures show the size distribution of particles in samples 1 and 2 with average sizes of ~4 nm and ~15 nm, respectively.

TEM images show that NPs produced by thermal decomposition method are small and present a narrow size distribution. Moreover, an additional annealing at 873 K

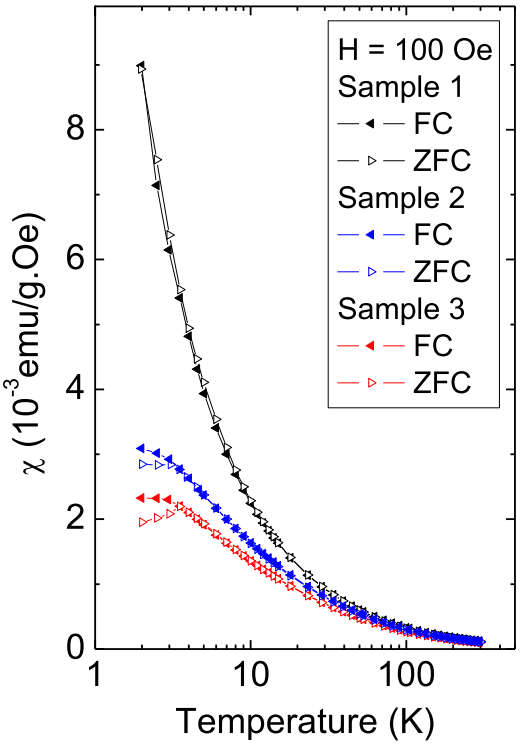

Figure 4. Temperature dependence of magnetic susceptibility (χ) for the two NP samples (black and blue lines) in comparison with the commercial sample (red line). Field-cooled (FC) data was obtained applying a magnetic field $H = 100$ Oe.

causes an increase in particle size with a loss in the NP shape uniformity.

3.2. Magnetization measurements

Magnetic susceptibility ($\chi = M/H$) with an applied field of $H = 100$ Oe, as a function of temperature is presented in figure 4. According to NAA Er concentration in samples 1 and 2 are $(23.5 \pm 0.8)\%$ and $(81.8 \pm 1.9)\%$ respectively. These values were used to normalize the magnetization values in order to obtain the effective magnetic moment at Er ions. No impurities were detected.

Magnetization measurements show irreversibility between the ZFC and FC curves for samples 2 and 3 below 3.1 K and 3.5 K respectively. These features are associated with the onset of the antiferromagnetically ordered state observed in the bulk material [8]. For sample 1, with the smallest NPs, the susceptibility shows a sharp increase at low temperatures (<20 K) when compared to the other two samples. This result is similar to that obtained for AFM CuO NPs and can be ascribed to uncompensated spins at the particles surface layer [22]. Particle diameter dependency of the magnetic susceptibility χ in AFM materials has been previously studied [22, 23] as well as changes in the Néel temperatures with particle size [24].

Figure 5 displays the dependence of the specific heat with temperature. All samples display clear peaks, which we associate to AFM phase transitions. For samples 3 and 2 the

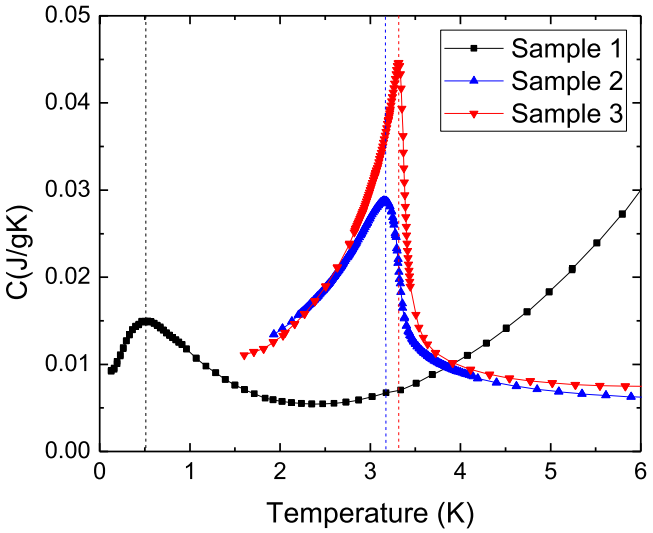

Figure 5. Temperature dependence of the specific heat for all samples. The dotted lines mark the Néel antiferromagnetic temperatures T_N.

temperature of the peaks at $T_N = 3.32$ K and 3.15 K, respectively, are in close agreement with the irreversibility temperatures observed in the magnetic susceptibility. Sample 1 shows a relatively broader peak centered at $T_N = 0.54$ K. This dependence of T_N on the particle size may come from surface effects. Due to the large ratio between surface area and volume in NPs, the surface effects have a significant contribution to magnetization. This contribution comes from defects on the surface resulting in uncompensated spins leading to surface magnetization, which can interact with the core magnetization [25]. Due to the defects, and low coordination, exchange interactions between surface atoms are weaker than those for core atoms, resulting in the AFM alignment in a lower temperature [24].

Figure 6 displays the magnetization M as a function of the applied magnetic field H measured at $T = 2$ K. From the results no hysteresis could be observed.

From the Curie–Weiss (CW) law for the temperature dependence on susceptibility, $\chi = \frac{C}{(T-\theta)}$, it is possible to determine CW temperature (θ_{CW}) and Curie constant (C) by considering the inverse of susceptibility, $\chi^{-1} = \frac{1}{C}T - \frac{\theta}{C}$, which can be fitted by a linear equation as displayed in figure 7.

From this linear fit, the CW temperature (θ_{CW}) and Curie constant (C) can be calculated. Effective magnetic moment is given by $\mu_{eff} = 2.828 \times \sqrt{C \times MM}\,\mu_B$, where MM is the molecular mass of erbium oxide ($MM_{Er2O3} = 382.518$ g mol^{-1}). Results from the fit along with μ_{eff} values are presented in table 1.

Results from table 1 show dependence between μ_{eff} values and particle size. The smaller the particle size is the higher is the effective magnetic moment. The value of the effective magnetic moment for sample 3 is in accordance with previous studies for Er_2O_3 bulk samples (9.58 μ_B) [26].

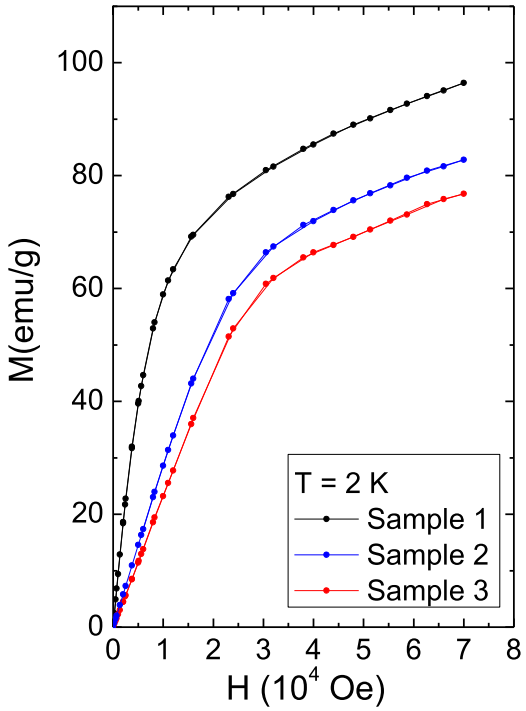

Figure 6. Magnetic field dependence on the magnetization for samples 1, 2 and 3. Measurements were carried out at 2 K. Neither hysteresis nor saturation is observed.

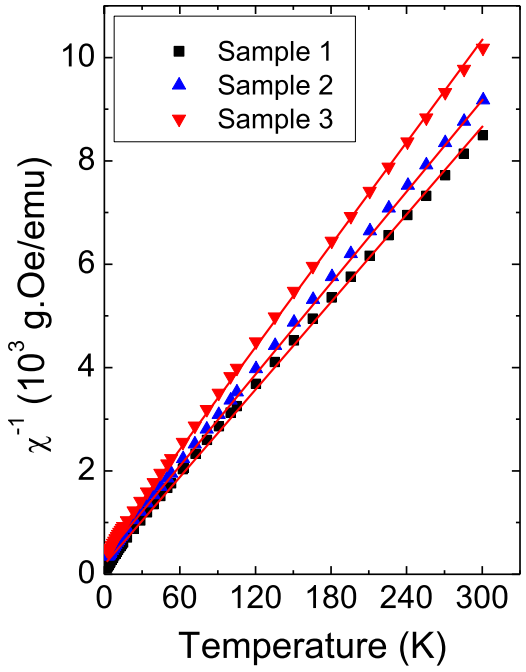

Figure 7. Inverse of the magnetic susceptibility χ^{-1} as a function of temperature. Solid lines are the Curie–Weiss law fitting.

3.3. NPs local properties—PAC

Perturbation function for 4 nm NPs (sample 1) is presented in figure 8.

According to previous studies [10, 14] very small NPs (under 10 nm) are difficult to be analyzed using PAC spectroscopy. Small NPs have sizes only few times the lattice parameter of the unit cell size with a very large surface area/volume ratio. Therefore, due to the surface influence, the position of atoms are slightly different from each other in most part of the particle, as it can be seen by the large peaks in XRD results. Because PAC is a technique highly dependent on distances with atomic resolution, these differences in atomic positions have a huge influence in the PAC spectrum modulation. Consequently, PAC spectrum measured at room temperature for sample 1 presents a broad frequency distribution as displayed in figure 8. This result is due to the small size of particles (around 5 nm). Considering that the lattice parameter is 1.05 nm and the particles are capped with an organic layer, the as-synthesized sample may contain a very small fraction of cationic sites at regular bixbyite structure. The PAC spectra were fitted considering ^{111}Cd probes occupying three different sites. The major fraction of probes presents a very broad quadrupole frequency $\nu_Q = 123(8)$ MHz and $\eta = 1.0$. The minor fraction has a broad $\nu_Q = 7(1)$ MHz with $\eta = 0$. Around 11% of probes present $\nu_Q = 147(8)$ MHz with $\eta = 0.59(6)$. The minor fractions of probes were assigned to be at the organic layer around the particles where the quadrupole interaction is expected to be very small. Thus, PAC measurements at different temperatures were performed only for sample 2. The annealing at 873 K was sufficient to remove almost all the organic material used as capping of particles with a consequent increase in the particle size.

Table 1. Average size, Néel Temperature (T_N), Curie constant (C), Curie–Weiss temperature (θ_{CW}) and effective magnetic moment (μ_{eff}) values for all samples obtained from χ^{-1} plot.

Sample	Average size (nm)	T_N (K)	C	θ_{CW} (K)	μ_{eff} (μ_B)
01	4.29	0.54	0.035	−6.64	10.41
02	14.99	3.15	0.034	−11.09	10.18
03	>100	3.32	0.030	−13.03	9.62

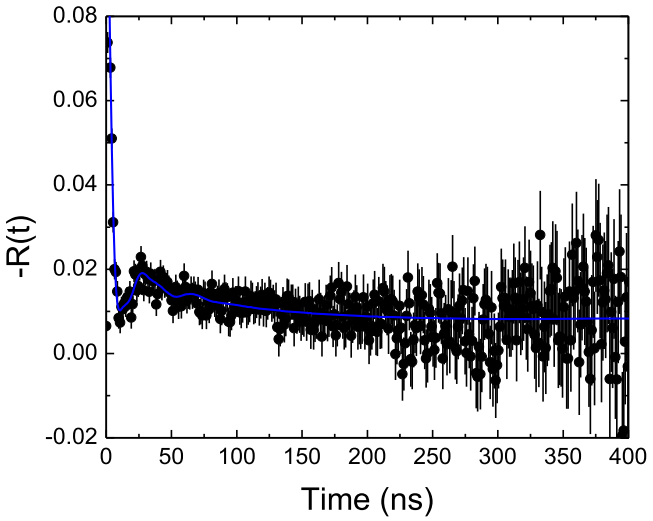

Figure 8. Perturbation function for sample 1 of Er_2O_3 measured with ^{111}In probe at room temperature.

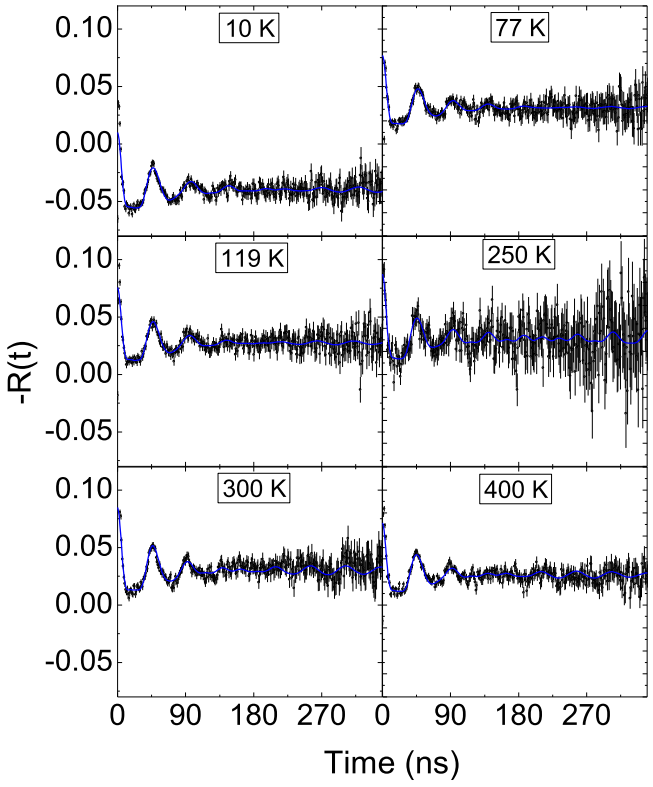

Figure 9. Perturbation function for sample 2 of Er_2O_3 measured with ^{111}In probe at different temperatures. Solid lines are the theoretical functions fitted to the experimental data using least squares method.

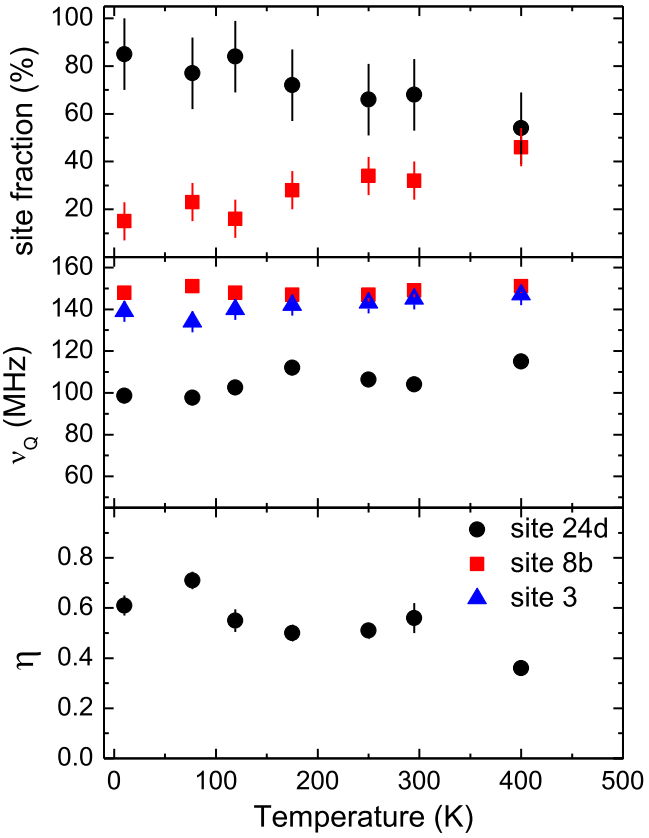

Figure 10. Site fractions, electric quadrupole frequency (ν_Q), and asymmetry parameter (η) as function of temperature for sample 2.

The PAC spectra for sample 2 (see figure 9) were fitted with a model considering pure EQI at ^{111}Cd probe nuclei occupying three site fractions, two of them corresponding to the expected crystalline sites (the asymmetric 24d and the symmetric 8b) for the bixbyite structure of Er_2O_3 [20].

The third site fraction (hereafter called site 3) with high population that increases with temperature from 69% at 10 K to 83% at 400 K was assigned to probes at the surface layer of particles. Probe nuclei at sites 8b and 24d are replacing Er ions at regular sites of Er_2O_3 in the core region of NPs. The population of the sites 8b and 24d were normalized taking into account the population of site 3. They are displayed in figure 10 along with the quadrupole frequency (ν_Q) obtained for the three sites and the asymmetry parameter for site 24d, since for sites 8b and sites 3, the fit yields $\eta = 0$.

Results at room temperature show that the symmetric sites 8b are occupied by a fraction of ~30(8)% of the probe nuclei characterized by $\nu_Q = 149(2)$ MHz, asymmetry parameter $\eta = 0$ and frequency distribution parameter $\delta = 1.4\%$. The asymmetric sites 24d are populated by ~70(15)% of the probe nuclei with $\nu_Q = 100(3)$ MHz, $\eta = 0.60(6)$ and $\delta = 6(2)\%$. Probes at sites 3 are characterized by a totally symmetric ($\eta = 0$) broad frequency $\nu_Q = 145(3)$ MHz.

Results of PAC measurements at room temperature using ^{111}Cd as probe nuclei in bulk samples of Er_2O_3 reported by Lupascu *et al* [20] show that sites 8b are occupied by 25% of the probe nuclei with $\nu_Q = 148.6(5)$ MHz and $\eta = 0$. Sites 24d were reported to be occupied by a population of 75% of probe nuclei with $\nu_Q = 82.0(5)$ MHz and $\eta = 0.823(5)$. The reported populations are those expected for a homogeneous occupation of probe nuclei substituting cation sites in the bixbyite structure.

The observed values of hyperfine parameters for the symmetric 8b sites in the present work are similar to those reported in the literature [20]. For the asymmetric 24d sites, the value of ν_Q is higher and the value of η is smaller than those reported for the bulk samples. The site fractions present the same population of bulk samples at low temperature, however, as temperature increases, the population of sites 8b increases as the population of sites 24d decreases (see the top graph in figure 10), reaching around 50% at 400 K. Interestingly, the quadrupole frequency of site 3 is similar to that of site 8b (see figure 10) also with $\eta = 0$.

Dopant impurities also have shown a preference to replace symmetric sites in the bixbyite structure [27]. However, in small systems, the size of particles is responsible for the observed behavior of the hyperfine parameters dependence on temperature. As temperature increases, the local structure of asymmetric 24d sites occupied by ^{111}Cd probes tend to relax to the symmetric 8b structure, exchanging the relative occupation of both sites. This tendency can also be observed in the behavior of η (see figure 10) that decreases when temperature increases. Moreover, ^{111}Cd probes at sites 3, ascribed to the surface layer of particles, present symmetric local structure with ν_Q similar to that for 8b sites. These results indicate that in small NPs with the bixbyite structure, asymmetric sites relax to the symmetric sites when temperature

increases. This supposition is supported by the tendency of probe population of both sites as displayed in figure 10 and by the results of sites 3 assigned to ^{111}Cd at the surface where structure is more relaxed.

4. Conclusions

In this study we have prepared small Er_2O_3 NPs by improving the traditional thermal decomposition method in a much shorter time using O_2 atmosphere. Structural and magnetic properties of the NP samples were investigated. NP samples were sufficiently small so that finite-size and surface effects could be observed. The smallest particles with average size of 4.29 nm presented a much higher magnetic susceptibility and effective magnetic moment when compared to those with 15 nm. PACs results showed that the local structure of particles relax to the symmetric 8b sites at the surface layer of particles as well as in the core, with the rise of the temperature increasing the relative population of sites 8b. The enhancement in the magnetic properties are, therefore, due to uncompensated spins in a large number of cationic sites because of the small size of particles, which favors a large ratio between surface area and volume, and due to the preference of symmetric sites that increases the polarization of magnetic ions.

Acknowledgments

To Fundação de Amparo à Pesquisa do Estado de São Paulo (FAPESP, grant 2014/14001-1) and Conselho Nacional de Desenvolvimento Científico e Tecnológico (CNPq, grants 164957/2013-8 and 473774/2013-5) for partial financial support and to master student Natalia M Nascimento for the help with nanoparticles synthesis. R S Freitas would like to acknowledge support from FAPESP (Grant 2015/16191-5).

ORCID iDs

Eduardo L Corrêa https://orcid.org/0000-0003-0819-3225
Artur W Carbonari https://orcid.org/0000-0002-4499-5949

References

[1] Xu C and Qu X 2014 Cerium oxide nanoparticle: a remarkably versatile rare earth nanomaterial for biological applications *NPG Asia Mater.* **6** e90
[2] Abdesselem M *et al* 2014 Multifunctional rare-earth vanadate nanoparticles: luminescent labels, oxidant sensors, and MRI contrast agents *ACS Nano* **8** 11126–37
[3] Stark W J, Stoessel P R, Wohllebenb W and Hafnerc A 2015 Industrial applications of nanoparticles *Chem. Soc. Rev.* **44** 5793–805
[4] Chinnasamya C N, Narayanasamya A, Ponpandiana N, Justin Joseyphusa R, Jeyadevanb B, Tohjib K and Chattopadhyay K 2002 Grain size effect on the Néel temperature and magnetic properties of nanocrystalline $NiFe_2O_4$ spinel *J. Magn. Magn. Mater.* **238** 281–7
[5] Thota S, Shim J H and Seehra M S 2013 Size-dependent shifts of the Néel temperature and optical band-gap in NiO Nanoparticles *J. Appl. Phys.* **114** 214307
[6] Bouzigues C, Gacoin T and Alexandrou A 2011 Biological applications of rare-earth based nanoparticles *ACS Nano* **5** 8488–505
[7] Mukherjee S, Chen C H, Chou C C, Tseng K F, Chaudhuri B K and Yang H D 2010 Colossal dielectric and magnetodielectric effect in Er_2O_3 nanoparticles embedded in a SiO_2 glass matrix *Phys. Rev.* B **82** 104107
[8] Narang V, Korakakis D and Seehra M S 2014 Nature of magnetism and magnetic-field-induced transitions in non-collinear antiferromagnet Er_2O_3 *J. Magn. Magn. Mater.* **368** 353–9
[9] Moon R M, Koehler W C, Child H R and Raubenheimer L J 1968 Magnetic structures of Er_2O_3 and Yb_2O_3 *Phys. Rev.* **176** 722
[10] Effenberger F B, Carbonari A W and Rossi L M 2016 The influence of 1,2-alkanediol on the crystallinity of magnetite nanoparticles *J. Magn. Magn. Mater.* **417** 49–55
[11] Shitu J, Wiarda D, Wenzel T, Uhrmacher M, Lieb K P, Bedi S and Bartos A 1992 Electric-field gradients in Sm_2O_3, Gd_2O_3, and Ho_2O_3 measured with perturbed-angular-correlation spectroscopy *Phys. Rev.* B **46** 7987–93
[12] Effenberger F B, Couto1 R A, Kiyohara P K, Machado G, Masunaga S H, Jardim R F and Rossi L M 2017 Economically attractive route for the preparation of high quality magnetic nanoparticles by the thermal decomposition of iron(III) acetylacetonate *Nanotechnology* **28** 115603
[13] Lima E Jr, De Biasi E, Mansilla M V, Saleta M E, Granada M, Troiani H E, Effenberger F B, Rossi L M, Rechenberg H R and Zysler R D 2013 Heat generation in agglomerated ferrite nanoparticles in an alternating magnetic field *J. Phys. D: Appl. Phys.* **46** 045002
[14] Correa E L, Bosch-Santos B, Cavalcante F H M, Correa B S, Freitas R S, Carbonari A W and Potiens M P A 2016 Properties of Gd_2O_3 nanoparticles studied by hyperfine interactions and magnetization measurements *AIP Adv.* **6** 056112
[15] De Soete D, Gijbels R and Hoste J 1972 *Neutron Activation Analysis* (New York: Wiley) p 856
[16] Bosch-Santos B, Carbonari A W, Cabrera-Pasca G A and Saxena R N 2014 Magnetic behavior of $LaMn_2(Si_{(1-x)}Ge_x)_2$ compounds characterized by magnetic hyperfine field measurements *J. Appl. Phys.* **115** 17E124
[17] Carbonari A W, Saxena R N, Pendl W Jr, Mestnik-Filho J, Atilli R N, Olzon-Dionysio M and de Souza S D 1996 Magnetic hyperfine field in the Heusler alloys Co_2YZ (Y = V, Nb, Ta, Cr; Z = Al, Ga) *J. Magn. Magn. Mater.* **163** 313–21
[18] Wiles D B and Young R A 1981 A new computer program for Rietveld analysis of x-ray powder diffraction patterns *J. Appl. Cryst.* **14** 149–51
[19] Malinovskii Y A and Bondareva O S 1991 Refined crystal structure of Er_2O_3 *Soviet Phys. Crystallogr. v.* **36** 882–3
[20] Lupascu D, Bartos A, Lieb K P and Uhrmacher M 1994 Precision PAC measurements in Er_2O_3 and Ho_2O_3 single crystals and structure refinement *Z. Phys.* B **93** 441–7
[21] Gu F, Wang S F, Lu M K, Zhou G J, Xu D and Yuan D R 2004 Photoluminescence properties of SnO_2 nanoparticles synthesized by sol–gel method *J. Phys. Chem.* B **108** 8119–23
[22] Punnoose A, Magnone H, Seehra M S and Bonevich J 2001 Bulk to nanoscale magnetism and exchange bias in CuO nanoparticles *Phys. Rev.* B **64** 174420–8
[23] Richardson J T, Yiagas D I, Turk B, Forster K and Twigg M V 1991 Origin of superparamagnetism in nickel oxide *J. Appl. Phys.* **70** 6977–82

[24] Blanusa J, Antic B, Kremenovic A, Nikolic A S, Mazzerolles L, Mentus S and Spasojevic V 2007 Particle size effect on Néel temperature in Er_2O_3 nanopowder synthesized by thermolysis of 2,4-pentadione complex *Solid State Commun.* **144** 310–4

[25] Issa B, Obaidat I M, Albiss B A and Haik Y 2013 Magnetic nanoparticles: surface effects and properties related to biomedicine applications *Int. J. Mol. Sci.* **14** 21266–305

[26] Knopf K and Waschkowski W 1997 Interaction of slow neutrons with natural terbium, holmium and erbium and its isotopes *Z. Phys.* A **357** 297–302

[27] Sena C, Costa M S, Muñoz E L, Cabrera-Pasca G A, Pereira L F D, Mestnik-Filho J, Carbonari A W and Coaquira J A H 2015 Charge distribution and hyperfine interactions in the vicinity of impurity sites in In_2O_3 doped with Fe, Co and Ni *J. Magn. Magn. Mater.* **387** 165–78